OPEN

Tuneable quantum spin Hall states in confined 1T' transition metal dichalcogenides

Biswapriyo Das[1*], Diptiman Sen[2] & Santanu Mahapatra[1]

Investigation of quantum spin Hall states in 1T' phase of the monolayer transition metal dichalcogenides has recently attracted the attention for its potential in nanoelectronic applications. While most of the theoretical findings in this regard deal with infinitely periodic crystal structures, here we employ density functional theory calculations and $k \cdot p$ Hamiltonian based continuum model to unveil the bandgap opening in the edge-state spectrum of finite width molybdenum disulphide, molybdenum diselenide, tungsten disulphide and tungsten diselenide. We show that the application of a perpendicular electric field simultaneously modulates the band gaps of bulk and edge-states. We further observe that tungsten diselenide undergoes a semi-metallic intermediate state during the phase transition from topological to normal insulator. The tuneable edge conductance, as obtained from the Landauer-Büttiker formalism, exhibits a monotonous increasing trend with applied electric field for deca-nanometer molybdenum disulphide, whereas the trend is opposite for other cases.

Topological insulators (TI)[1–4] have emerged as a relatively new quantum state of matter, characterized by gapped (insulating) bulk states and gapless (highly conducting) edge/surface states according to the bulk-boundary correspondence. The 'topological' attribute in this context is the nontrivial topology of the bulk bands spanned by their characteristic electron wavefunctions. Since this nontrivial topology is a characteristic of the gapped energy states, in order to flip the topology across the interface, either the energy gap has to be closed or the symmetry property protecting the edge/surface states has to be broken. Appearance of gapless edge (2D) or surface (3D) states at the interface of a TI and a normal insulator (NI) or vacuum is thus the most fundamental property of a topologically nontrivial phase.

Quantum spin Hall insulators (QSHI) or 2D TIs, as originally proposed by Kane and Mele[5,6], features spin-polarized 'helical' edge states with opposite momentum on each side of the sample to form a Kramer's pair. According to Kane and Mele[5], graphene was predicted to be a QSHI with a finite gap opening at Dirac point due to spin-orbit coupling (SOC). Unfortunately, very weak SOC in graphene rendered it impossible to experimentally verify their prediction. However, in 2006, the existence of quantum spin Hall (QSH) state was theoretically predicted by Bernevig, Hughes and Zhang (BHZ)[7] and later experimentally demonstrated by König *et al.*[8] for HgTe/CdTe quantum wells. Thenceforth several other 2D TI materials have been reported such as InAs/GaSb[9,10] quantum wells, bismuthene[11,12], functionalized Bi/Sb films[13], monolayer BiX/SbX (X = H, F, Cl and Br)[14], 2D bismuth arsenic (BiAs)[15], arsenene[16], arsenene oxide[17], monolayer AsSb[18], phosphorene[19], silicon-based chalcogenide (Si$_2$Te$_2$)[20], 2D transition-metal halides[21], monolayer ZrTe$_5$ and HfTe$_5$[22], Cu$_2$Te and Ag$_2$Te[23], silicene[24,25], germanene[26,27], 2D SiGe[28], stanene[29], functionalized stanene[30], tellurene[31] etc. This apart, a recent high-throughput density functional theory (DFT) based study has reported[32] thirteen new 2D materials that are candidates for QSHI such as AsCuLi$_2$, Pt$_2$HgSe$_3$ etc. While experimental realization of many of these 2D materials is still in infancy, recent advancements in technology have aided the growth and fabrication of several such new and exotic materials with interesting quantum properties[33,34]. However, monolayer transition metal dichalcogenides (TMD), i.e. MX$_2$ where M and X denotes metal (e.g. Mo, W etc.) and chalcogen (e.g. S, Se, Te etc.) atoms respectively, were first predicted to possess the topological properties by Qian *et al.*[35] and later it was verified by several other investigations[36–48]. Based on first principles calculations and tight-binding Hamiltonian, they demonstrated[35] that among several polytypic structures, 1T' phase of a monolayer TMD features band inversion in its bulk energy spectrum. It is caused by the formation of periodic doubling of metal chain in 1T' structures and large SOC of

[1]Nano-Scale Device Research Laboratory, Department of Electronic Systems Engineering, Indian Institute of Science (IISc) Bangalore, Bangalore, 560012, India. [2]Centre for High Energy Physics, Indian Institute of Science (IISc) Bangalore, Bangalore, 560012, India. *email: biswapriyodas1@gmail.com

transition metals opens a band gap at the otherwise gapless Dirac points. They depicted the edge-state energy spectrum for $1T'$ MoS$_2$ using surface Green's function calculations and demonstrated that topological phase transition in these materials can be achieved as a result of external perturbations like electric field or strain. However, experimental findings on the other hand indicate that the topological properties of these materials can also be tuned by temperature[38] and surface doping[41]. Later the Haeckelite crystal structures[49] of monolayer TMDs were also found to possess topological characteristics. To be precise, time-reversal symmetry (TRS) protected topological phases in these monolayer $1T'$ TMDs are attributed by $\mathbb{Z}_2$ topological invariant, where $\mathbb{Z}_2 = 0$ indicates topologically trivial phase and $\mathbb{Z}_2 = 1$ denotes topologically 'twisted' state or QSH state. The nontrivial topology necessarily dictates the transport through edge states to be free of elastic back-scattering, thereby effectuating the edge conductance to be exactly equal to the conductance quantum e^2/h, where e and h denotes electronic charge and Planck's constant respectively.

However, from an engineering viewpoint, it is highly desirable to devise a method to control the transport through edge states by external means which forms the notion of topological insulator field effect transistors (TIFET)[50]. The most straightforward solution would be rapidly introducing and removing the edge states through topological phase transition, which for $1T'$ TMDs has been demonstrated by applying vertical electric field[35,36] and strain[35]. Even, if the TRS is broken either by external perturbation (e.g. magnetic field[44]) or due to the presence of magnetic impurities[51–53] or through 'spontaneous' breaking[37] by the presence of non-zero magnetic moment, the existence of edge states is also not guaranteed or even if they exist, the conductance may deviate from the quantized value. In this article, we investigate another possible way to modulate the edge conductance, which is by confining the material geometry. Previously, Zhou et al.[54] have reported a gap opening in edge state spectrum as a result of the restriction on strip width and showed that the charge conductance gets modified as a function of the energy gap.

Here, in order to investigate the effects of quantum confinement on the edge state spectra and charge conductance of monolayer $1T'$ TMDs, we have employed a continuum model based analytical approach rather than using surface Green's function formalism. Such analytical approach would be suitable for developing compact device models for 2D TIFETs. First, we study the topological properties of four such TMD materials, to be precise, MoS$_2$, MoSe$_2$, WS$_2$ and WSe$_2$. We obtain the bulk band structures of these materials using density functional theory (DFT) computations and thereby investigate the Rashba splitting of spin-degenerate bands as a consequence of external electric field. We then identify the critical field values for these materials which define the quantum critical points for topological phase transitions. Thereafter we calibrate a $k \cdot p$ Hamiltonian that accurately captures the band structure subtleties of $1T'$ TMDs and represent a continuum modeling approach to obtain the edge state spectrum. We introduce the finite size effect by confining the real space geometry of the material, by virtue of which, the edge states from opposite edges couple together to introduce a gap in the edge spectrum thereby transforming the massless linear Dirac dispersions to massive Dirac hyperbolas. For confined structures, the edge conductance is found to be less than the conductance quantum and it decreases with increasing degree of confinement. It is also found that the edge conductance can be tuned as a function of external electric field only for finite width of the strips, whereas for unconfined geometry it maintains a constant value of e^2/h for all electric fields.

Results

Crystal structure and bulk energy dispersion. Monolayer TMDs are known to possess several polytypic structures e.g. $1H$ (trigonal prismatic coordination), $1T$ (octahedral coordination) and $1T'$ (distorted $1T$ structure), among which, $1T$ phase, owing to its dynamical instability[35,55,56], undergoes a spontaneous lattice distortion to transform into stable $1T'$ structure. Probably the most subtle feature of this $1T'$ phase is the inverted bandgap at the Brillouin zone center (Γ), that occurs as a consequence of periodic doubling of transition metal chain, lowering the metal d orbitals below chalcogen p orbitals in the energy scale. Shown in Fig. 1(a,b) are the crystal structures and rectangular first Brillouin zone (FBZ) of $1T'$ TMD. The FBZ has four time-reversal invariant momentum (TRIM) points, labeled in Fig. 1(b) as Γ, X, Y and L, while the fundamental bandgap appears at a point Λ along the k_x axis. First-principles based calculations were conducted (see methods for details) for the aforesaid TMD materials in order to probe their electronic band structures. The bulk energy dispersions of $1T'$ MoS$_2$ under varying perpendicular electric fields are depicted in Fig. 1(c–f) and the same for $1T'$ WSe$_2$ are shown in Fig. 1(g–j), while dispersions of MoSe$_2$ and WS$_2$ in $1T'$ phase can be found in Supplementary Figs. 1 and 2 respectively. For all of these bulk dispersion profiles the Fermi energy is set to zero. In comparison to $1T'$ MoS$_2$, the topmost valence band of WSe$_2$ is 'flatter' owing to its heavier hole effective mass (see Table 1). Figure 1(c) depicts the band structure of monolayer $1T'$ MoS$_2$ in absence of external electric field. For $1T'$ TMDs, the electronic contribution to the valence and conduction bands near Γ point mainly comes from metal d and chalcogen p orbitals respectively, indicating a band inversion[35] at zone center with an inverted bandgap of $\delta = \delta_p + \delta_d$, where δ_p and δ_d are corresponding energies of lowest conduction and highest valence bands at Γ point with respect to zero energy level. The Dirac-like linear dispersion (represented by black dotted lines) appears at Λ point along $\Gamma - X$ direction in absence of SOC and the role of high SOC of the transition metal atoms is to introduce a finite energy gap (E_g) at Λ making the bulk system gapped. Numeric values of E_g, δ_p and δ_d for the four TMD materials are tabulated in Table 1, which are in good agreement with the previously reported[35] data. The external electric field is applied along out-of-plane z direction by introducing an electric potential shift between two metallic electrodes residing on opposite sides of the monolayer TMD material which is spaced out form them by sufficiently thick vacuum isolations. We denote the electric field in the vacuum region as F_{VAC} and in the monolayer TMD as F_{ML} and calculate these quantities following the method prescribed by Jelver et al.[37]. The application of vertical electric field effectuates a strong Rashba splitting of the otherwise degenerate valence and conduction bands near the fundamental band gap as illustrated in Fig. 1(d–f,h–j). As a result, the bulk band gap decreases and at a particular value of F_{ML}, called the critical electric field for topological phase transition (F_C), the
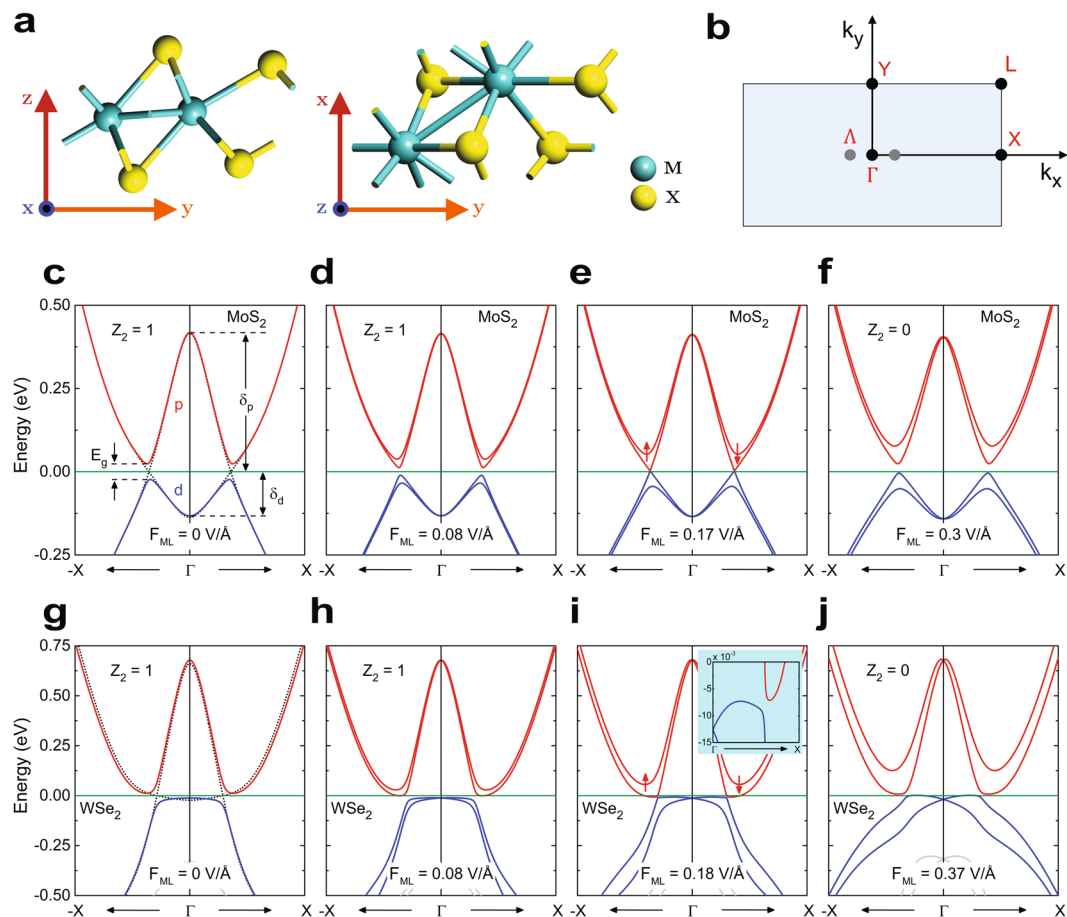
Figure 1. (**a**) Crystal structure of a $1T'$ MX_2, where M and X denote metal (e.g. Mo, W etc.) and chalcogen (e.g. S, Se, Te etc.) atoms respectively. The $1T'$ structure is formed by lattice distortion of dynamically unstable $1T$ structure. (**b**) First Brillouin zone of $1T'$ MX_2, showing the high-symmetry points Γ, X, Y and L. Γ is the zone centre where the bulk energy dispersion undergoes a band inversion. The fundamental band gap occurs at a point Λ along the k_x axis. (**c**–**f**) Illustrate the bulk band structures of MoS_2 respectively under the electric fields $F_{ML} = 0, 0.08, 0.17$ and 0.3 V/Å. In all of these figures red lines represent conduction bands and blue lines represent valence bands. The Fermi level, set to zero, is represented by green line. (**c**) Depicts that near Γ point the conduction band is mainly contributed by p orbitals of sulphur and valence band is mainly composed of d orbitals of molybdenum indicating band inversion. The effect of spin-orbit coupling is to open an energy gap near the Λ point in the otherwise gapless bulk dispersion. The black dotted line in (**c**) indicates the dispersion without considering SOC. The inverted band gap δ is the sum of contributions from conduction $\left(\delta_p\right)$ and valence $\left(\delta_d\right)$ bands. As shown in (**d**–**f**), the effect of external electric field is to introduce Rashba splitting between spin-degenerate bands thereby lifting the degeneracy. As the field strength is increased, eventually the band gap closes at $F_{ML} = 0.17$ V/Å and in response to further increase in F_{ML}, the gap reopens with degeneracy remaining lifted. The states in (**c**) and (**d**) are topological with $\mathbb{Z}_2 = 1$ and the state in (**f**) is topologically trivial ($\mathbb{Z}_2 = 0$). However in (**e**), the topological invariant is ill-defined indicating the quantum critical point for topological phase transition. (**g**) – (**j**) demonstrate the similar characteristics of bulk energy dispersions for WSe_2. The colour scheme for representation is same as stated before. However, it can be seen in the inset of (**i**) that as the electric field approaches the critical value, WSe_2 tends to become an indirect semiconductor.

	δ_p (eV)	δ_d (eV)	E_g (eV)	$\frac{m_x^p}{m_0}$	$\frac{m_y^p}{m_0}$	$\frac{m_x^d}{m_0}$	$\frac{m_y^d}{m_0}$	v_1 ($\times 10^5$ m/s)	v_2 ($\times 10^5$ m/s)	α (eÅ)
MoS_2	−0.417	−0.132	0.047	0.29	0.48	0.92	2.32	0.230	3.383	0.159
$MoSe_2$	−0.719	−0.041	0.030	0.17	0.28	3.14	2.65	0.285	3.421	0.272
WS_2	−0.145	−0.023	0.046	0.28	0.53	8.20	3.20	0.845	2.931	0.173
WSe_2	−0.678	−0.012	0.023	0.16	0.36	8.40	3.28	0.380	3.542	0.241

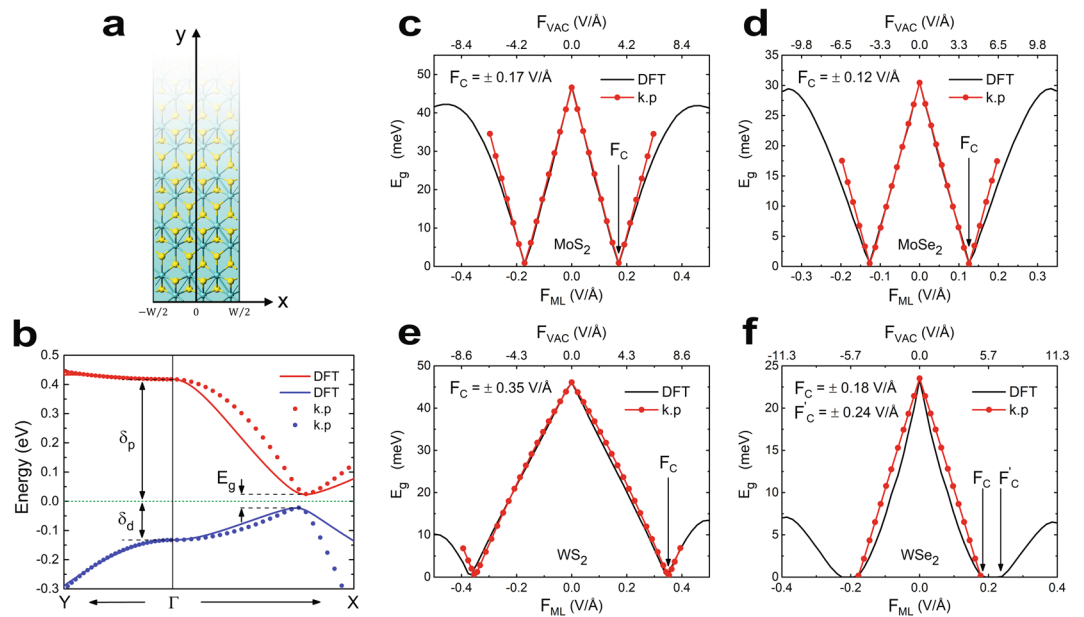**Table 1.** Material-specific parameters. m_0 is the rest mass of electron.

Figure 2. (**a**) Sample geometry under study, where the width is limited to W in x direction whereas it is infinite in y direction. (**b**) Calibration of the $k.p$ Hamiltonian against the data obtained from DFT calculations. Here the red lines represent conduction band and blue lines represent valence band, whereas, the solid and dotted lines respectively indicate the results obtained from DFT calculations and data obtained after calibrating the $k.p$ Hamiltonian. The Fermi level, set to zero, is represented by green dashed line. (**c–f**) Demonstrate the topological phase transition of MoS_2, $MoSe_2$, WS_2 and WSe_2 respectively as a result of applied electric field. In (**c–f**), black solid lines represent the DFT data and red lines with data markers represent the $k.p$ Hamiltonian. The critical electric fields F_C were found to be ± 0.17 V/Å, ± 0.12 V/Å, ± 0.35 V/Å and ± 0.18 V/Å respectively for MoS_2, $MoSe_2$, WS_2 and WSe_2. (c) – (f) also showcase the calibration of bulk band gaps of respective materials obtained from analytical formulation with the corresponding DFT data. The material specific electrical parameter α was obtained from these calibrations. However, as shown in (f), WSe_2 acquires an intermediate semi-metallic phase for $F_C \leq |F_{ML}| \leq F'_C$ during the transition from topological to non-topological state. The concerned $k.p$ Hamiltonian fails to describe this intermediate state.

dispersion becomes gapless. The numeric values of F_C for MoS_2, $MoSe_2$, WS_2 and WSe_2 were found to be ± 0.17 V/Å, ± 0.12 V/Å, ± 0.35 V/Å and ± 0.18 V/Å respectively. The numeric value of $F_C = \pm 0.17$ V/Å as obtained for MoS_2 is slightly different form previously reported data[35], which may originate from different simulation methodologies. However, for $F_{ML} > F_C$, the band gap reopens at the Λ point along Γ – X direction, but the spin degeneracy remains lifted. Inside the regime $|F_{ML}| < F_C$, all four of $1T'$ MX_2 under consideration are topologically non-trivial ($\mathbb{Z}_2 = 1$) and outside that regime, i.e. for $|F_{ML}| > F_C$ the phase becomes trivial ($\mathbb{Z}_2 = 0$). However, exactly at $F_{ML} = \pm F_C$, the quantum phase is ill-defined because the bulk spectra in this case becomes gapless. Based on parity criteria of the valence bands, the $\mathbb{Z}_2$ indices for all of these materials were calculated by Qian et $al.$[35]. The existence of topological phase for $|F_{ML}| < F_C$ will be verified in the following section by probing the edge state spectrum. Although the electric field has similar effects on all four $1T'$ TMDs, viz. MoS_2, $MoSe_2$, WS_2 and WSe_2, it was found that WSe_2 tends to become an indirect semiconductor as F_{ML} reaches $\pm F_C$ as shown in the inset of Fig. 1(i).

Sample geometry and topological phase transition. In order to investigate the effects of real-space confinement on topological phases, we consider the sample geometry as illustrated in Fig. 2(a), where the sample length is infinite along y direction, but width of the material has been limited to W in x direction. It is to be noted that by the term 'edge', throughout the article we represent only that type of physical termination where TRS is preserved. Also the absence of any form of magnetic perturbation (e.g. introduction of magnetic impurities) in our model implies that TRS is always preserved. The spatial confinement of material geometry severely affects the edge-state dispersion by introducing an energy gap in the otherwise gapless edge spectra. For analytical calculation of edge state spectrum, a low energy $k.p$ Hamiltonian (see methods) was calibrated with the bulk dispersion, obtained from self-consistent DFT calculations as shown in Fig. 2(b) for MoS_2. Details of the calibration procedure is provided in the methods section. Figure 2(c–f) demonstrate the topological phase transitions of all materials as well as comparison between the numeric values of their bulk bandgaps as obtained from DFT computations and analytical calculations from $k.p$ Hamiltonian. It signifies that the Hamiltonian accurately describes the low-energy spectrum of the bulk. Although the Hamiltonian works well within the electric fields $\pm F_C$ (which defines the quantum critical point for topological phase transition), it deviates from the actual result
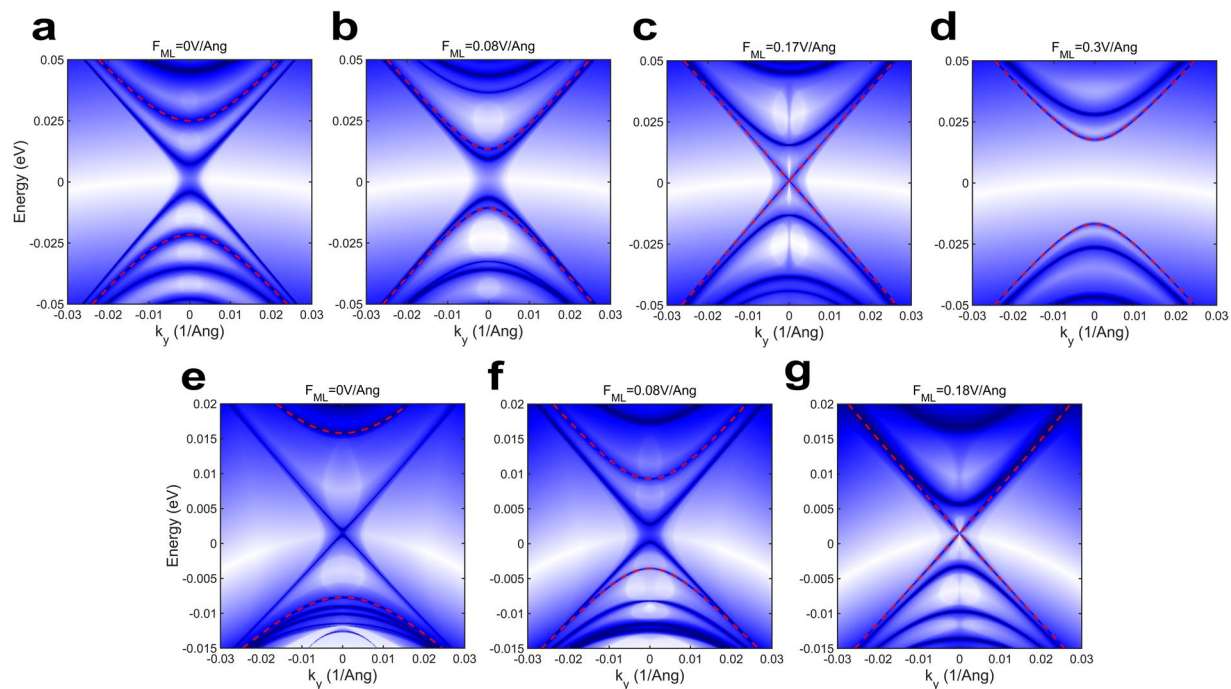
Figure 3. (**a–d**) are the energy spectra of edge states for $1T'$ MoS$_2$ ribbon with a width of 20 nm. In all of these figures, we have plotted the functional values of coupled Eqs. (6) and (9) for given range of k_y and E. While the color changes from white to blue to dark, the functional values change from very high to medium to zero. Therefore, the dark lines correspond to valid solutions for the energy bands. The red dashed lines correspond to bulk dispersion and the edge state dispersions can be identified as dark lines in between bulk valence and conduction bands. As shown in the figures, the effect of finite width is to introduce a gap in the otherwise gapless edge state spectrum and only when the width is small and finite, the applied electric field is able to modulate this energy gap. At $F_{ML} = 0.17$ V/Å, the edge states become indistinguishable from the bulk spectra indicating the phase transition point. In (**d**), $F_{ML} = 0.3$ V/Å, which is larger than the critical field for MoS$_2$ and consequently, the phase becomes topologically trivial. Edge states vanish in this case. (**e–g**) Represent the edge state spectra of a WSe$_2$ ribbon of width 10 nm. The colour scheme is the same as stated above. Similar arguments as stated before for MoS$_2$ hold true for WSe$_2$ also, except for the fact that energy spectrum for electric fields greater (or smaller) than the critical field of WSe$_2$ could not be obtained since the Hamiltonian becomes invalid in that regime.

as F_{ML} goes far beyond $\pm F_C$. However, it was observed that unlike other three TMDs under consideration, WSe$_2$ acquires an intermediate semi-metallic gapless state during the transition from topological to non-topological phase. This semi-metallic phase appears in the regime $F_C \leq |F_{ML}| \leq F'_C$, where F'_C is the critical electric field for semi-metallic to non-topological phase transition. However, the $k \cdot p$ Hamiltonian under consideration assumes that the bulk band gap can be closed only at one particular electric field (either positive or negative), i.e. it indicates the presence of only two quantum critical points $\pm F_C$. Therefore the Hamiltonian fails to describe this intermediate phase of WSe$_2$.

Effect of confinement on topological insulators.   It is well known that the most subtle characteristic of a 2D TI material is the existence of chiral edge states on opposite edges of the bulk. In general, these edge states are gapless and thus their dispersions can be modeled by massless Dirac-like linear equations. On the contrary, confining the material geometry introduces a gap (E_{gE}) in the otherwise gapless edge state spectrum which increases exponentially with decreasing W and their massless Dirac-like linear dispersions get transformed into massive Dirac hyperbolas[54]. The edge-state energy spectra of a $1T'$ MoS$_2$ ribbon with $W = 20$ nm as calculated (see methods for details) from the $k \cdot p$ Hamiltonian, are presented in Fig. 3(a–d) for increasing values of F_{ML}. Here, the solid dark areas denote valid solutions for energy eigenvalues. The red dashed lines represent the highest valence and lowest conduction bands of the bulk and the edge states can be identified as isolated dark solid lines within the bulk energy gap (although in some cases the edge states may become indistinguishable from the bulk as discussed later). As mentioned earlier, due to the finite width effect, the edge state dispersion becomes gapped for $F_{ML} < F_C$ and the gap appears exactly at $k_y = 0$. As shown in Fig. 3(a–b), the edge state is well defined for the electric fields $F_{ML} = 0$ V/Å and $F_{ML} = 0.08$ V/Å, which are less than F_C. At the critical field (i.e. $F_{ML} = F_C = 0.17$ V/Å), however, the edge state spectrum becomes gapless ($E_{gE} = 0$) and it coincides with the bulk dispersion. If F_{ML} is further increased beyond F_C (or decreased beyond $-F_C$), the edge states vanish and the phase becomes topologically trivial (i.e. NI phase), which is depicted in Fig. 3(d) where $F_{ML} = 0.3$ V/Å. Similar dispersions of edge states under varying F_{ML} for WSe$_2$ strip ($W = 10$ nm) are shown in Fig. 3(e–g). However, in this case, the
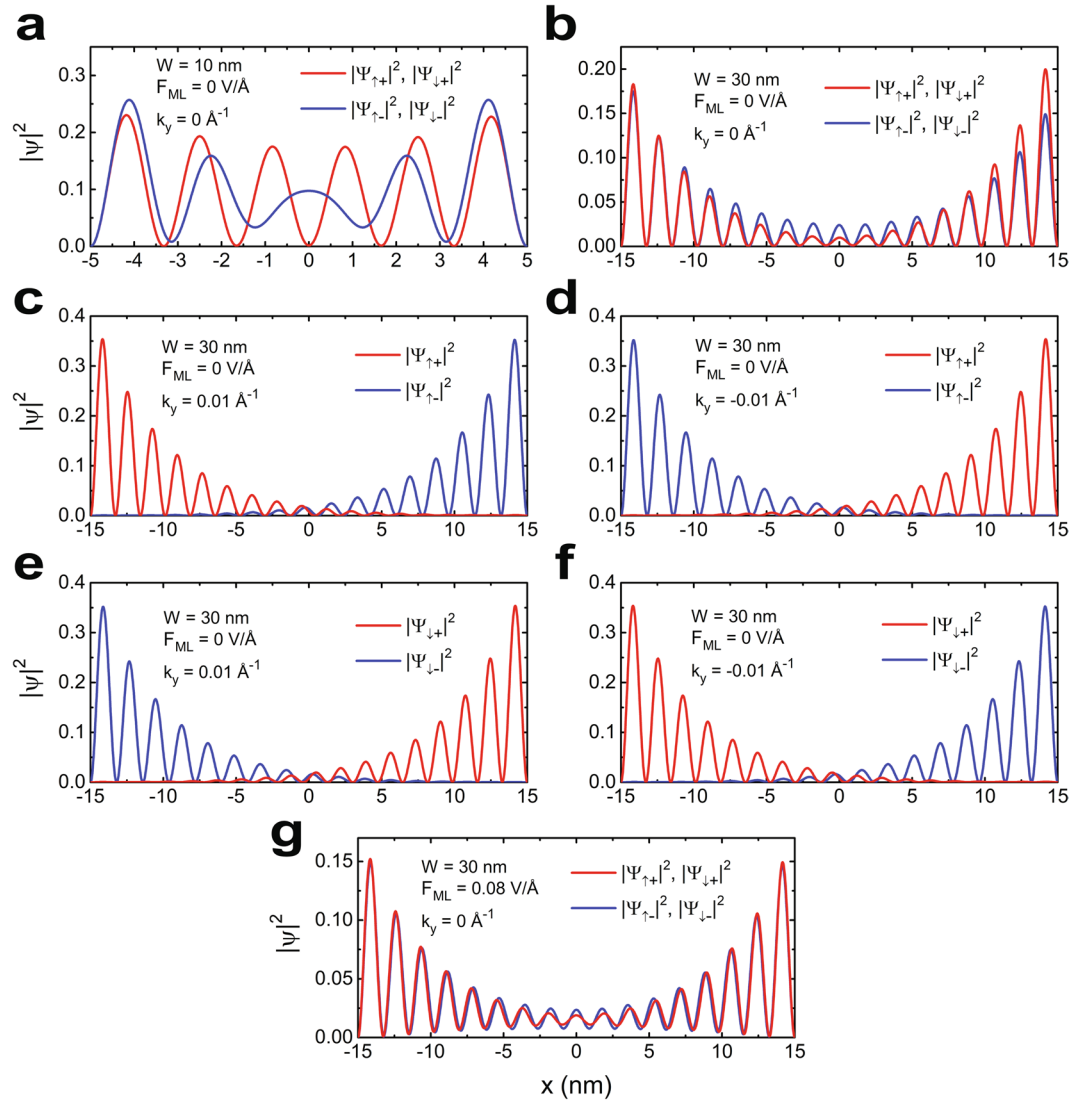
Figure 4. (**a,b**) Depict the probability density profiles of the edge state wavefunctions $\Psi_{\uparrow\pm}$ and $\Psi_{\downarrow\pm}$ for 10 nm and 30 nm wide MoS_2 ribbons respectively. It shows that for $k_y = 0$, the densities are symmetrically distributed across the space, while increased overlap between the wavefunctions for 10 nm indicates the effect of confinement. (**c,d**) Are respectively the density distribution profiles of spin-up states for $k_y = \pm 0.01$ V/Å and (**e,f**) are the same for spin-down states with $k_y = \pm 0.01$ V/Å. (**c–f**) Illustrate that the spin texture gets resolved as we move away from the centre. (**g**) Indicates that electric field does not have any significant effect on the edge state wavefunctions.

energy spectrum for $F_{ML} > 0.18$ V/Å could not be obtained since the proposed $k \cdot p$ Hamiltonian becomes invalid as mentioned earlier. It is further observed that edge band gap E_{gE} gets modulated as a function of F_{ML} and this is true only for samples with finite width because for an infinite sample ($W = \infty$) the edge-spectrum is always gapless. Thus, the role of electric field is to introduce or remove the edge states, i.e. to effectuate topological phase transition and the effect of finite width is to make $E_{gE} > 0$ thereby enabling its modulation. Hence, in a nutshell, E_{gE} can be independently controlled and modulated as a function of F_{ML} and W which is later demonstrated in detail. The edge state spectra for $MoSe_2$ and WS_2 can be found in Supplementary Figs. 3 and 4 respectively.

For a single edge of a TI material, the energy gap cannot be opened in the edge state spectra unless TRS is broken. However, the gap opening in our findings is a direct consequence of spatial overlap of the edge state wavefunctions (Ψ) from opposite sides of a finite-width sample. For infinite widths or when $W \gg \lambda^{-1}$ (λ is the length scale of the wavefunction), the edge state wavefunctions are dominantly distributed near the edges of the material and corresponding probability densities ($|\Psi|^2$) rapidly decay inside the bulk. However, when W becomes comparable to or smaller than λ^{-1}, these wavefunctions from opposite edges can indeed overlap in space and couple together to open a gap in edge state dispersion (see methods for details). Thus for spatially confined systems with $W \leq \lambda^{-1}$, the edge state spectra can become gapped even though TRS is preserved. For example, we find $W < 50$ nm causes significant overlap between the edge state wavefunctions of MoS_2. To support this statement, probability densities of the normalized edge state wavefunctions of $1T'$ MoS_2 have been plotted in Fig. 4(a,b) respectively
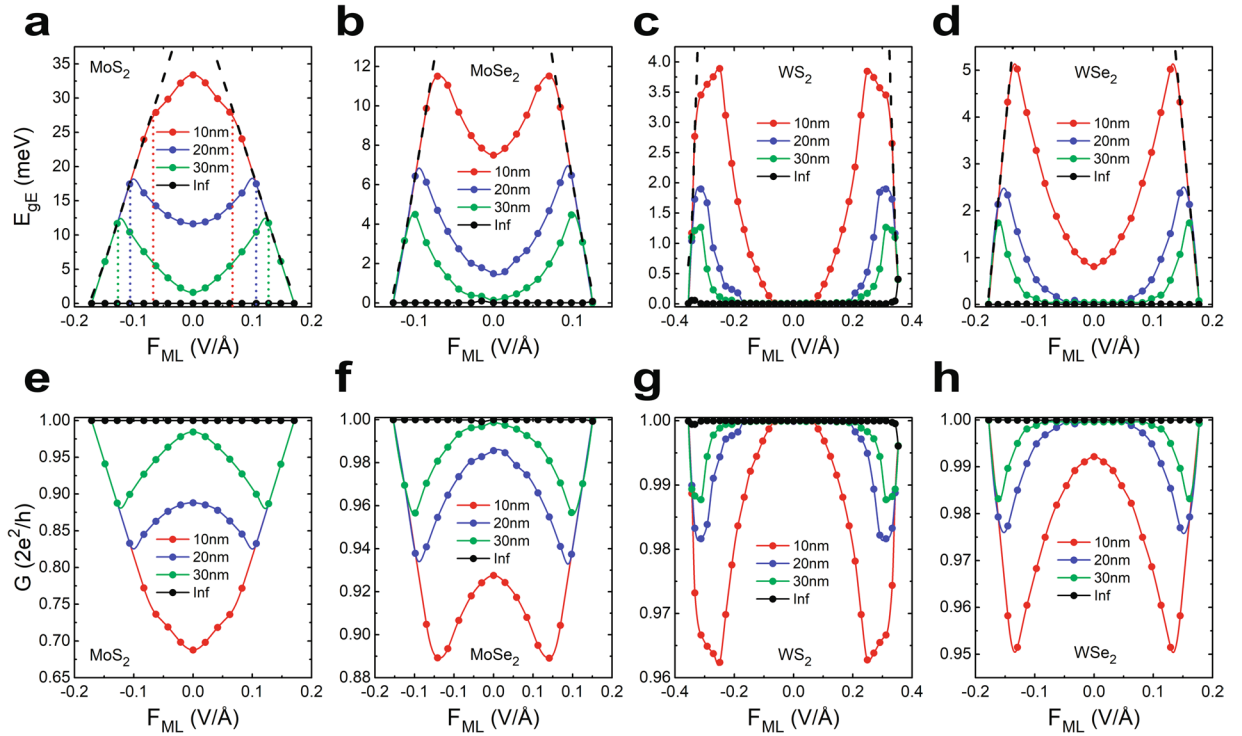
Figure 5. (**a–d**) Demonstrate the variation of edge state band gap E_{gE} as a function of the monolayer electric field F_{ML} for the materials MoS_2, $MoSe_2$, WS_2 and WSe_2 respectively. In all of these plots, the black dashed lines indicate the bulk band gap profile with respect to the field strength. The red, blue, green and black lines with data markers respectively indicate the results obtained for the sample widths 10 nm, 20 nm, 30 nm and infinite. To be noted from these figures is that for any particular field strength, E_{gE} increases with increasing degree of confinement. Also the 'effective critical field' gets reduced with decreasing ribbon width. (**e–h**) Showcases the charge conductance profiles for the respective materials. The color scheme of representation is same as mentioned before. G attains its maximum value of $2e^2/h$ for infinitely wide sample and it gets modulated by F_{ML} only when the ribbon-width is finite.

for 10 nm and 30 nm sample widths in absence of electric field. As shown in Fig. 4(a,b), at $k_y = 0$, all the density profiles are symmetrically distributed on both sides with $|\Psi_{\uparrow+}|^2 = |\Psi_{\downarrow+}|^2$ and $|\Psi_{\uparrow-}|^2 = |\Psi_{\downarrow-}|^2$ where $\Psi_{\uparrow+}$, $\Psi_{\downarrow+}$ are respectively spin-up ($\sigma_x = 1$) and spin-down ($\sigma_x = -1$) electron wavefunctions for conduction band while $\Psi_{\uparrow-}$, $\Psi_{\downarrow-}$ are respectively the same for valence band with σ_x being the first Pauli matrix. As stated earlier, the wavefunctions for finite widths do not vanish far away from the edges in the bulk, rather they overlap in space. This overlap occurs between $\Psi_{\uparrow\pm}(x, +k_y)$ and $\Psi_{\uparrow\pm}(x, -k_y)$, and also between similar spin-down states. As shown in Fig. 4(a), the overlap is more pronounced for $W = 10$ nm than $W = 30$ nm, causing larger E_{gE} for smaller width. It is also noted that the spin texture of the edge states is not resolved at $k_y = 0$. Figure 4(c–f) depicts the probability densities of the same wavefunctions at $k_y = \pm 0.01$ Å^{-1} with $W = 30$ nm and $F_{ML} = 0$ V/Å. Quite obviously, the spin texture is resolved in this case as $k_y \neq 0$. Therefore, for any non-zero k_y, the states $\Psi_{\uparrow+}(x, +k_y)$ and $\Psi_{\uparrow-}(x, -k_y)$ have the same spin texture and positive velocity ($v_y > 0$) and the density distribution is dominant on one side; whereas $\Psi_{\uparrow+}(x, -k_y)$ and $\Psi_{\uparrow-}(x, k_y)$ have same spin texture and negative velocity ($v_y < 0$) and the density distribution is dominant on other side. The spin-down states also behave in a similar fashion. Nevertheless, near $k_y = 0$ the wavefunctions couple together due to spatial confinement and the densities of $\Psi_{\uparrow\pm}(x, k_y = 0)$ and $\Psi_{\downarrow\pm}(x, k_y = 0)$ are distributed symmetrically on both sides, which explains the opening of energy gap in edge state spectrum exactly at $k_y = 0$. However, the external electric field does not have any significant impact on the edge state wavefunctions other than increasing the amplitude of $|\Psi|^2$ near $x = 0$ as shown in Fig. 4(g).

Figure 5(a–d) represent the variation of E_{gE} as a function of F_{ML} ($-F_C \leq F_{ML} \leq F_C$) with W as a parameter (ranging from 10 nm to infinite) respectively for the $1T'$ phases of MoS_2, $MoSe_2$, WS_2 and WSe_2. Here the black dashed lines indicate the variation of bulk band gap with respect to F_{ML} of the corresponding material. It clarifies that E_{gE} cannot be tuned at all with the electric field for an infinitely wide sample. However, except for the case of deca-nanometer MoS_2, for a given finite width, E_{gE} increases monotonically with increasing $|F_{ML}|$ until it meets the bulk band gap profile. Figure 5(a–d) also reveals that for any particular F_{ML}, E_{gE} increases with increasing degree of confinement. Interestingly, the most peculiar characteristic is that for a given small and finite W, E_{gE} coincides with E_g, i.e. the edge states become indistinguishable from bulk bands at an electric field much lower (higher) than F_C ($-F_C$) and it becomes more prominent with decreasing values of W. This can be regarded as a reduction of effective F_C for a small finite width, where F_C actually defines the critical field for infinite geometry. These 'effec-

tive critical fields' for $1T'$ MoS$_2$ are marked with colored dotted lines in Fig. 5(a). Thus for a TMD material with small W, such phase with an electric field between 'effective critical field' and F_C becomes somewhat ambiguous in topological parlance. This apart, it is also observed that for materials with heavy electron effective mass (viz. WS$_2$ and WSe$_2$), the edge state spectra remain gapless at zero electric field even when the sample width is very small. For example, as shown in Fig. 5(c), E_{gE} for WS$_2$ remains zero in absence of electric field even when $W = 10$ nm. Similar observations for WSe$_2$ can be made from Fig. 5(d) when $W \geq 20$ nm. This is because the length scale of the wavefunctions i.e. λ is a complex function of electron effective masses (viz. m_x^p, m_y^p, m_x^d and m_y^d) and thus the characteristic λ^{-1} becomes smaller for a material with heavier effective mass.

As the edge states deviate from their ideal linear dispersions owing to spatial confinement of strip geometry, the charge conductance (G) through them should also get modified accordingly. Theoretically, the ideal charge conductance of a QSH phase is $2e^2/h$ because of the presence of two chiral 1D conducting channels at the edges of the QSH strip[8]. Following the Landauer-Büttiker formula (see methods), the numeric values of G were calculated for the gapped edge states in all four materials and are presented in Fig. 5(e–h). It is noteworthy that G is very sensitive to the variations of E_{gE}. As shown in these figures, G attains the maximum value of $2e^2/h$ when the width is infinite, but it gradually decreases with decreasing W. Nevertheless, the charge conductance can only be tuned by the external field when W is finite. Figure 5(e–h) demonstrate that for a given finite W, the conductance profile decreases (with deca-nanometer MoS$_2$ being an exception) from its maximum attainable value at $F_{ML} = 0$ V/Å with increasing $|F_{ML}|$ until $|F_{ML}|$ takes the value of 'effective critical field' for that width of that particular material.

Discussion

Using first-principles based calculations and by employing a calibrated $k \cdot p$ Hamiltonian, we have studied the effect of spatial confinement and external electric field on the QSH states in four monolayer $1T'$ TMD materials viz. MoS$_2$, MoSe$_2$, WS$_2$ and WSe$_2$. We find that the vertical electric field effectuates a topological phase transition in these materials at a particular field strength, called the critical electric field and thus it is responsible for turning the edge states 'on' or 'off'. We also find that unlike the other three materials, $1T'$ WSe$_2$ acquires an intermediate semi-metallic phase during the topological phase transition. However, infinite geometry of the materials renders it impossible to modulate the edge state dispersion by applying the vertical electric field. On the contrary, spatial confinement of material geometry opens a band gap in the otherwise gapless edge state spectrum, caused by the coupling between overlapping wavefunctions from opposite edges of the material. It also enables the external field to modulate the edge spectra and thereby the charge conductance. In this case, the charge conductance may deviate from its ideal value of $2e^2/h$. Finally, we conclude that the effect of confinement may prove to be a way to engineer the charge conductance through edge states, which may become useful for designing a TIFET.

Methods

First-principles based atomistic computations. First-principles based calculations for all four monolayer $1T'$ TMDs were carried out using the DFT code as implemented in QuantumATK[57] in conjunction with generalized gradient approximation exchange correlation for non-collinear SOC (SOGGA) and Perdew-Burke-Ernzerhof (PBE) functional[58]. We have employed fully relativistic SG15[59,60] (SG15-SO) norm-conserving pseudo-potentials as implemented in QuantumATK database along with corresponding LCAO (linear combination of atomic orbitals) basis set of 'medium' accuracy for all elements. We also selected the fermion occupation method to be gaussian smearing with the electron temperatures 595 K, 1625K, 880 K and 600 K for MoS$_2$, MoSe$_2$, WS$_2$ and WSe$_2$ respectively. For Brillouin zone integration, the Monkhorst-Pack[61] k-point samplings were set to $13 \times 13 \times 1$ and $11 \times 11 \times 1$ for MoS$_2$ and MoSe$_2$ respectively and $7 \times 7 \times 1$ for WS$_2$ and WSe$_2$ along with the density mesh cutoff energy being 90 Hartree for MoS$_2$ and MoSe$_2$, 400 Hartree for WS$_2$ and 180 Hartree for WSe$_2$. Maximum iteration steps for self-consistent calculations were set to 200 using Pulay mixer algorithm and we followed the fast Fourier transform (FFT) for Poisson solver. Furthermore, sufficient vacuum region of about 15 Å was provided in z direction to all the structures in order to avoid spurious interactions between periodic images. The geometry optimization of unit cells of these materials including the effects of SOC were performed using LBFGS (Limited-memory Broyden-Fletcher-Goldfarb-Shanno) optimizer[62] with maximum stress error tolerance of 0.001 eV/Å^3 and force tolerance of 0.01 eV/Å. However, in presence of finite electric field, the geometry optimization in QuantumATK with SG15-SO pseudopotentials including the effects of SOC is a formidable task and computationally way more resource-intensive, which often develops convergence issues. Therefore the optimization of unit cells were only limited to the case of zero electric field. Nevertheless, the electric field should have negligible impact on the ionic positions as mentioned in the supplementary material of ref. [35]. In order to investigate the effects of electric field, two metal electrodes are inserted along z direction on either sides of the material with sufficient vacuum isolations, whereby an electric potential difference in these electrodes induces the electric field F_{ML} in the monolayer TMD. Thereafter, self-consistent calculations were carried out using multi-grid Poisson solver with Dirichlet boundary condition set to the z direction.

Nevertheless, despite all the atomistic calculations were carried out using PBE functional, the bulk band structures of all four $1T'$ TMDs at zero electric field, obtained using Heyd-Scuseria-Ernzerhof (HSE)[63] hybrid functional as implemented in the VASP[64,65] code are presented in Supplementary Fig. 5 for sake of comparison.

Development of $k.p$ Hamiltonian based continuum model. We start with a low-energy $k.p$ Hamiltonian $\left(H_{k.p}\right)$ for monolayer $1T'$ MX$_2$ structures, as prescribed by Qian et al.[35] and Liu et al.[36] that follows the form:

$$H_{k.p} = \begin{pmatrix} E_p(k_x, k_y) & 0 & -iv_2\hbar k_y & v_1\hbar k_x \\ 0 & E_p(k_x, k_y) & v_1\hbar k_x & -iv_2\hbar k_y \\ iv_2\hbar k_y & v_1\hbar k_x & E_d(k_x, k_y) & 0 \\ v_1\hbar k_x & iv_2\hbar k_y & 0 & E_d(k_x, k_y) \end{pmatrix}$$

(1)

where $E_p(k_x, k_y) = -\delta_p - \frac{\hbar^2 k_x^2}{2m_x^p} - \frac{\hbar^2 k_y^2}{2m_y^p}$ and $E_d(k_x, k_y) = \delta_d + \frac{\hbar^2 k_x^2}{2m_x^d} + \frac{\hbar^2 k_y^2}{2m_y^d}$ with $\hbar$ being the modified Planck's constant, m_x^p, m_y^p, m_x^d and m_y^d being corresponding effective masses in conduction (p) and valence (d) bands in x and y directions respectively and v_1, v_2 are respectively the velocities along x and y directions. E_p and E_d basically denote the onsite energies of p and d orbitals respectively and the upper and lower $2{\times}2$ blocks along the off-diagonal of $H_{k.p}$ define the inter-band interactions between them. Numeric values of δ_p and δ_d were directly obtained from the DFT data while the effective masses and velocities were obtained by calibrating the above Hamiltonian with DFT results. All of these material-specific parameters can be found in Table 1. In our calculation $\delta(\delta_p + \delta_d) < 0$ represents the band inversion at Γ point.

Numerical fitting of $H_{k.p}$ with the data obtained from first-principles calculations was carried out for both $\Gamma \rightarrow X$ and $\Gamma \rightarrow Y$ directions in the FBZ using nonlinear least-squares method in conjunction with trust-region-reflective optimization algorithm[66,67]. Since precise fitting is required around both Γ and Λ points, it is necessary to identify a region around the Γ point which is just sufficient to include Λ. point. Thereby, about 0.2 Å^{-1} around the Γ point in both X and Y directions was chosen for curve-fitting. It was observed that although the Hamiltonian fits nicely in the $\Gamma \rightarrow Y$ direction, it fits poorly beyond Λ point along the $\Gamma \rightarrow X$ direction, which becomes more prominent for the materials with heavy electron effectiv mass such as WS$_2$ and WSe$_2$.

To incorporate the effects of external electric field, i.e. the Rashba splitting of spin-degenerate bands, we consider the electric field Hamiltonian[36] as:

$$H_F = \alpha F_{ML} \begin{pmatrix} 0 & 0 & 1 & 0 \\ 0 & 0 & 0 & 1 \\ 1 & 0 & 0 & 0 \\ 0 & 1 & 0 & 0 \end{pmatrix}$$

(2)

where F_{ML} is the monolayer electric field induced by the potential difference between the electrodes and α is a material-specific electrical constant. Thus the total Hamiltonian of $1T'$ MX$_2$ including the effect of electric field becomes:

$$H = H_{k.p} + H_F$$

(3)

By fitting the band gap as obtained from the eigenvalues of H against the band gap computed by DFT (see Fig. 2(c–f)), we get the numeric values of α for different materials as tabulated in Table 1.

We start the analytical derivation of edge state spectra by rewriting H as:

$$H = (\delta^- I - \delta^+ \tau_z) - (M_x^- I + M_x^+ \tau_z)k_x^2 - (M_y^- I + M_y^+ \tau_z)k_y^2 + v_1\hbar k_x \tau_x \sigma_x + v_2\hbar k_y \tau_y + \alpha F_{ML}\tau_x$$

(4)

where, $\delta^\pm = (\delta_d \pm \delta_p)/2$ and $M_{x(y)}^\pm = \frac{\hbar^2}{4}\left[\frac{1}{m_{x(y)}^p} \pm \frac{1}{m_{x(y)}^d}\right]$. Here I stands for identity matrix, and the 4×4 matrices $\sigma_x, \tau_x, \tau_y, \tau_z$ are mathematically represented as:

$$\sigma_x = \begin{pmatrix} 0 & 1 & 0 & 0 \\ 1 & 0 & 0 & 0 \\ 0 & 0 & 0 & 1 \\ 0 & 0 & 1 & 0 \end{pmatrix}, \quad \tau_x = \begin{pmatrix} 0 & 0 & 1 & 0 \\ 0 & 0 & 0 & 1 \\ 1 & 0 & 0 & 0 \\ 0 & 1 & 0 & 0 \end{pmatrix}, \quad \tau_y = \begin{pmatrix} 0 & 0 & -i & 0 \\ 0 & 0 & 0 & -i \\ i & 0 & 0 & 0 \\ 0 & i & 0 & 0 \end{pmatrix}, \quad \tau_z = \begin{pmatrix} 1 & 0 & 0 & 0 \\ 0 & 1 & 0 & 0 \\ 0 & 0 & -1 & 0 \\ 0 & 0 & 0 & -1 \end{pmatrix}$$

The last term in Eq. (4) describes the electric field. For this Hamiltonian in Eq. (4), σ_x can be found to be a good quantum number that has the eigenvalues ± 1. Hence in σ_x basis, the spin texture can be resolved and the 4×4 Hamiltonian H can be separated into two 2×2 Hamiltonians corresponding to each eigenvalue of σ_x. We nomenclate $\sigma_x = +1$ states as 'spin-up' states ($\psi_\uparrow$) and $\sigma_x = -1$ states as 'spin-down' states ($\psi_\downarrow$). Now, let us consider only the spin-up Hamiltonian that reads:

$$H_\uparrow = \begin{pmatrix} -\delta_p - \dfrac{\hbar^2 k_x^2}{2m_x^p} - \dfrac{\hbar^2 k_y^2}{2m_y^p} & v_1\hbar k_x - iv_2\hbar k_y + \alpha F_{ML} \\[2mm] v_1\hbar k_x + iv_2\hbar k_y + \alpha F_{ML} & \delta_d + \dfrac{\hbar^2 k_x^2}{2m_x^d} + \dfrac{\hbar^2 k_y^2}{2m_y^d} \end{pmatrix}$$

(5)

Therefore the eigenvalue problem for spin-up states becomes $\hat{H}_\uparrow \psi_\uparrow = E\psi_\uparrow$ with E being the energy eigenvalue and $\psi_\uparrow$ being a two-component wavefunction $\psi_\uparrow = \begin{pmatrix} \psi_1 \\ \psi_2 \end{pmatrix}$. For a strip geometry of width W (see Fig. 2(a)), only k_y

is a good quantum number and k_x should be replaced by Peierls substitution $k_x = -i\partial/\partial x$. Now, in order to obtain the energy spectrum and wavefunctions, we solve the coupled Schrödinger equations using the trial wavefunctions $\psi_{1,2} = e^{\lambda x}\begin{pmatrix} 1 \\ 1 \end{pmatrix}$. The resulting secular equation reads

$$\begin{vmatrix} \left(-\delta_p - \dfrac{\hbar^2 k_y^2}{2m_y^p} - E\right) + \dfrac{\hbar^2}{2m_x^p}\lambda^2 & -iv_2\hbar k_y + \alpha F_{ML} - iv_1\hbar\lambda \\[4mm] iv_2\hbar k_y + \alpha F_{ML} - iv_1\hbar\lambda & \left(\delta_d + \dfrac{\hbar^2 k_y^2}{2m_y^d} - E\right) - \dfrac{\hbar^2}{2m_x^d}\lambda^2 \end{vmatrix} = 0 \tag{6}$$

It gives four roots of λ, namely $\lambda_1, \lambda_2, \lambda_3$ and λ_4. The nature of λ_ns $(n = 1, 2, 3, 4)$ determine the distribution of wavefunction in space. If λ_ns are purely imaginary, then the wavefunctions can be expressed in terms of sine and cosine functions, i.e. they span throughout the whole space indicating solutions for bulk states. But when λ_ns become real quantities, the wavefunctions are mainly distributed near the edges and they rapidly decay inside the bulk, pointing out the existence of edge states. However, in our calculation, λ_ns were found to be complex numbers with non-zero real part and therefore the resulting wavefunctions become oscillatory as well as exponentially decaying away from the edges (see Fig. 4). In general, the secular equation (Eq. (6)) turns out to be a depressed quartic equation in presence of external electric field. Nevertheless, at $F_{ML} = 0$, it transforms into a simple quadratic equation. Next, we figure out the eigenfunctions ψ_1 and ψ_2 as functions of λ_n as:

$$\psi_1(\lambda_n) = 1$$
$$\psi_2(\lambda_n) = \frac{\left(-\delta_p - \dfrac{\hbar^2 k_y^2}{2m_y^p} - E\right) + \dfrac{\hbar^2}{2m_x^p}\lambda_n^2}{iv_2\hbar k_y - \alpha F_{ML} + iv_1\hbar\lambda_n} \tag{7}$$

Taking their linear combination, therefore we may construct the wavefunction as:

$$\psi_\uparrow = \sum_{n=1}^{4} C_n \exp(\lambda_n x)\begin{pmatrix} \psi_1(\lambda_n) \\ \psi_2(\lambda_n) \end{pmatrix} \tag{8}$$

where C_ns $(n = 1, 2, 3, 4)$ are the coefficients for linear combination. Now, applying the open boundary condition $\psi_\uparrow(x = \pm W/2, k_y) = 0$, we get another secular equation from the condition of having a nontrivial solution of these coefficients, that takes the following form.

$$\sum_{j=1}^{3} \Theta_j(\lambda_1, \lambda_2, \lambda_3, \lambda_4) = 0 \tag{9}$$

The expressions for $\Theta_j(j = 1, 2, 3)$ are given as:

$$\begin{aligned}
\Theta_1 &= \sinh\left[\frac{W}{2}(\lambda_1 - \lambda_2)\right] \times \sinh\left[\frac{W}{2}(\lambda_3 - \lambda_4)\right] \times \{\psi_2(\lambda_1)\psi_2(\lambda_2) + \psi_2(\lambda_3)\psi_2(\lambda_4)\} \\
\Theta_2 &= -\sinh\left[\frac{W}{2}(\lambda_1 - \lambda_3)\right] \times \sinh\left[\frac{W}{2}(\lambda_2 - \lambda_4)\right] \times \{\psi_2(\lambda_1)\psi_2(\lambda_3) + \psi_2(\lambda_2)\psi_2(\lambda_4)\} \\
\Theta_3 &= \sinh\left[\frac{W}{2}(\lambda_2 - \lambda_3)\right] \times \sinh\left[\frac{W}{2}(\lambda_1 - \lambda_4)\right] \times \{\psi_2(\lambda_2)\psi_2(\lambda_3) + \psi_2(\lambda_1)\psi_2(\lambda_4)\}
\end{aligned} \tag{10}$$

Finally, the energy spectrum of the edge states can be obtained by numerically solving Eqs. (6) and (9) (see Fig. 3). The MATLAB code used to produce the dispersions in Fig. 3 is given in Supplementary Data. The same formalism can be applied to get the solutions for spin-down $(\sigma_x = -1)$ states. However, as it suggests, the dispersions for spin-up and spin-down states were found to be degenerate.

On the other hand, to obtain the edge-state wavefunctions, we need the numeric values of the coefficients C_n. If we choose C_1 to be unity, then from the condition of having nontrivial solutions of the other three coefficients we can get the analytical expressions for C_2, C_3 and C_4 as noted below.

$$C_1 = 1$$
$$C_2 = -\frac{\beta\exp\left[\frac{W}{2}(\lambda_4 - \lambda_2)\right] + \beta'\exp\left[\frac{W}{2}(\lambda_3 - \lambda_2)\right] + \exp\left[\frac{W}{2}(\lambda_1 - \lambda_2)\right]}{1 + \gamma\exp\left[\frac{W}{2}(\lambda_4 - \lambda_2)\right] + \gamma'\exp\left[\frac{W}{2}(\lambda_3 - \lambda_2)\right]}$$
$$C_3 = \beta' + \gamma'C_2$$
$$C_4 = \beta + \gamma C_2 \tag{11}$$

where, β, β', γ and γ' are expressed as:

$$\beta = \frac{\psi_2(\lambda_1)\sinh\left[\frac{W}{2}(\lambda_3 - \lambda_1)\right]}{\psi_2(\lambda_4)\sinh\left[\frac{W}{2}(\lambda_4 - \lambda_3)\right]} \quad , \quad \beta' = \frac{\psi_2(\lambda_1)\sinh\left[\frac{W}{2}(\lambda_4 - \lambda_1)\right]}{\psi_2(\lambda_3)\sinh\left[\frac{W}{2}(\lambda_3 - \lambda_4)\right]}$$

$$\gamma = \frac{\psi_2(\lambda_2)\sinh\left[\frac{W}{2}(\lambda_3 - \lambda_2)\right]}{\psi_2(\lambda_4)\sinh\left[\frac{W}{2}(\lambda_4 - \lambda_3)\right]} \quad , \quad \gamma' = \frac{\psi_2(\lambda_2)\sinh\left[\frac{W}{2}(\lambda_4 - \lambda_2)\right]}{\psi_2(\lambda_3)\sinh\left[\frac{W}{2}(\lambda_3 - \lambda_4)\right]}$$

(12)

Finally, the normalized wavefunctions for $\sigma_x = +1$ can be written as:

$$\Psi_\uparrow(x, k_y) = N e^{ik_y y} \sum_{n=1}^{4} C_n \exp(\lambda_n x)\begin{pmatrix} \psi_1(\lambda_n) \\ \psi_2(\lambda_n) \end{pmatrix}$$

(13)

where N is the normalization constant. Again, using the same formalism as stated above, $\Psi_\downarrow(x, k_y)$ can also be calculated.

Nevertheless, this formalism also applicable for an infinite sample provided appropriate boundary conditions have been incorporated which are: $\psi(x = 0, k_y) = 0$ and $\psi(x = -\infty, k_y) = 0$.

Calculation of charge conductance through edge states. The charge conductance G through the edge states gets modified as an effect of gap opening in dispersion profile. Following the Landauer-Büttiker formula[54,68], the charge conductance was calculated as

$$G = \frac{2e^2}{h}\left[1 + \frac{1}{1 + e^{\left[(E_{gE}/2) - E_F\right]/k_B T}} - \frac{1}{1 + e^{\left[-(E_{gE}/2) - E_F\right]/k_B T}}\right]$$

(14)

where, E_F is the Fermi energy (set to zero), k_B is Boltzmann's constant and T is temperature. To be specific, all the conductance profiles in Fig. 5 were calculated for $T = 300$ K and it was assumed that no disorder is present in the sample. Thus the conductance appears to be a linear function of E_{gE}, which will be highly nonlinear at low temperatures. It clearly indicates that when the spectrum is gapless, i.e. $E_{gE} = 0$, then G attains its maximum value of $2e^2/h$ and it reduces with increasing E_{gE}. Nevertheless, the conductance profile becomes quantized at absolute zero.

Data availability
The authors declare that the main data supporting the findings of this study are available within the article and its supplementary information documents. Other relevant data are available from the corresponding author upon request.

Code availability
MATLAB code for simulating dispersion spectra is shared in Supplementary Data.

References
1. Hasan, M. Z. & Kane, C. L. Colloquium: Topological insulators. *Rev. Mod. Phys.* **82**, 3045–3067 (2010).
2. Moore, J. E. The birth of topological insulators. *Nature* **464**, 194–198 (2010).
3. Qi, X.-L. & Zhang, S.-C. Topological insulators and superconductors. *Rev. Mod. Phys.* **83**, 1057–1110 (2011).
4. Schnyder, A. P., Ryu, S., Furusaki, A. & Ludwig, A. W. W. Classification of topological insulators and superconductors in three spatial dimensions. *Phys. Rev. B.* **78**, 195125 (2008).
5. Kane, C. L. & Mele, E. J. Quantum Spin Hall Effect in Graphene. *Phys. Rev. Lett.* **95**, 226801 (2005).
6. Kane, C. L. & Mele, E. J. Z_2 Topological Order and the Quantum Spin Hall Effect. *Phys. Rev. Lett.* **95**, 146802 (2005).
7. Bernevig, B. A., Hughes, T. L. & Zhang, S.-C. Quantum Spin Hall Effect and Topological Phase Transition in HgTe Quantum Wells. *Science* **314**, 1757–1761 (2006).
8. König, M. *et al*. Quantum Spin Hall Insulator State in HgTe Quantum Wells. *Science* **318**, 766–770 (2007).
9. Liu, C., Hughes, T. L., Qi, X.-L., Wang, K. & Zhang, S.-C. Quantum Spin Hall Effect in Inverted Type-II Semiconductors. *Phys. Rev. Lett.* **100**, 236601 (2008).
10. Du, L., Knez, I., Sullivan, G. & Du, R.-R. Robust Helical Edge Transport in Gated InAs/GaSb Bilayers. *Phys. Rev. Lett.* **114**, 096802 (2015).
11. Murakami, S. Quantum Spin Hall Effect and Enhanced magnetic Response by Spin-Orbit Coupling. *Phys. Rev. Lett.* **97**, 236805 (2006).
12. Sawahata, H., Yamaguchi, N. & Ishii, F. Electric-field-induced Z_2 topological phase transition in strained single bilayer Bi(111). *Appl. Phys. Express* **12**, 075009 (2019).
13. Li, S.-S., Ji, W.-X., Hu, S.-J., Zhang, C.-W. & Yan, S.-S. Effect of Amidogen Functionalization on Quantum Spin Hall Effect in Bi/Sb(111) Films. *ACS Appl. Mater. Interfaces* **9**, 41443–41453 (2017).
14. Song, Z. *et al*. Quantum spin Hall insulators and quantum valley Hall insulators of BiX/SbX (X = H, F, Cl and Br) monolayers with a record bulk band gap. *NPG Asia Materials* **6**, e147 (2014).
15. Teshome, T. & Datta, A. Phase coexistence and strain-induced topological insulator in two-dimensional BiAs. *J. Phys. Chem. C* **122**, 15047–15054 (2018).
16. Zhang, H., Ma, Y. & Chen, Z. Quantum spin Hall insulators in strain-modified arsenene. *Nanoscale* **7**, 19152 (2015).
17. Wang, Y.-P. *et al*. Two-dimensional arsenene oxide: A realistic large-gap quantum spin Hall insulator. *Appl. Phys. Lett.* **110**, 213101 (2017).

18. Nie, Y., Rahman, M., Wang, D., Wang, C. & Guo, G. Strain induced topological phase transitions in monolayer honeycomb structures of group-V binary compounds. *Scientific Reports* **5**, 17980 (2015).
19. Liu, Q., Zhang, X., Abdalla, L. B., Fazzio, A. & Zunger, A. Switching a normal insulator into a topological insulator via electric field with application to phosphorene. *Nano Lett.* **15**, 1222–1228 (2015).
20. Zhang, R.-W. *et al*. Silicon-based chalcogenide: Unexpected quantum spin Hall insulator with sizable band gap. *Appl. Phys. Lett.* **109**, 182109 (2016).
21. Zhou, L. *et al*. New family of quantum spin Hall insulators in two-dimensional transition-metal halide with large nontrivial band gaps. *Nano Lett.* **15**, 7867–7872 (2015).
22. Weng, H., Dai, X. & Fang, Z. Transition-metal pentatelluride ZrTe$_5$ and HfTe$_5$: A paradigm for large-gap quantum spin Hall insulators. *Phys. Rev. X* **4**, 011002 (2014).
23. Ma, Y., Kou, L., Dai, Y. & Heine, T. Two-dimensional topological insulators in group-11 chalcogenide compounds: M_2Te (M = Cu, Ag). *Phys. Rev. B* **93**, 235451 (2016).
24. Ezawa, M. Valley-Polarized Metals and Quantum Anomalous Hall Effect in Silicene. *Phys. Rev. Lett.* **109**, 055502 (2012).
25. Ezawa, M. Spin valleytronics in silicene: Quantum Spin Hall-quantum anomalous Hall insulators and single-valley semimetals. *Phys. Rev. B* **87**, 155415 (2013).
26. Zhang, L. *et al*. Structural and Electronic Properties of Germanene on MoS$_2$. *Phys. Rev. Lett.* **116**, 256804 (2016).
27. Amlaki, T., Bokdam, M. & Kelly, P. J. Z_2 Invariance of Germanene on MoS$_2$ from First Principles. *Phys. Rev. Lett.* **116**, 256805 (2016).
28. Teshome, T. & Datta, A. Topological insulator in two-dimensional SiGe induced by biaxial tensile strain. *ACS Omega* **3**, 1–7 (2018).
29. Tang, P. *et al*. Stable two-dimensional dumbbell stanene: A quantum spin Hall insulator. *Phys. Rev. B* **90**, 121408(R) (2014).
30. Zhang, R.-W. *et al*. Ethynyl-functionalized stanene film: a promising candidate as large-gap quantum spin Hall insulator. *New J. Phys.* **17**, 083036 (2015).
31. Zhang, W. *et al*. Topological phase transitions driven by strain in monolayer tellurium. *Phys Rev B* **98**, 115411 (2018).
32. Marrazzo, A., Gibertini, M., Campi, D., Mounet, N. & Marzari, N. Relative abundance of Z_2 topological order in exfoliable two-dimensional insulators. *Nano Lett.* **19**, 8431–8440 (2019).
33. Zhu, F.-F. *et al*. Epitaxial growth of two-dimensional stanene. *Nature Materials* **14**, 1020 (2015).
34. Zhang, S.-J. *et al*. Intrinsic Dirac half-metal and quantum anomalous Hall phase in a hexagonal metal-oxide lattice. *Phys. Rev. B* **96**, 205433 (2017).
35. Qian, X., Liu, J., Fu, L. & Li, J. Quantum spin Hall effect in two-dimensional transition metal dichalcogenides. *Science* **346**, 1344–1347 (2014).
36. Liu, L. & Guo, J. Assessment of performance potential of MoS$_2$-based topological insulator field-effect transistors. *J. Appl. Phys.* **118**, 124502 (2015).
37. Jelver, L., Stradi, D., Stokbro, K., Olsen, T. & Jacobsen, K. W. Spontaneous breaking of time-reversal symmetry at the edges of $1T'$ monolayer transition metal dichalcogenides. *Phys. Rev. B.* **99**, 155420 (2019).
38. Berger, A. N. *et al*. Temperature-driven topological transition in $1T'$-MoTe$_2$. *npj Quantum. Materials* **3**, 2 (2018).
39. Fang, Y. *et al*. Discovery of Superconductivity in $2M$ WS$_2$ with Possible Topological Surface States. *Adv. Mater.* **31**, 1901942 (2019).
40. Ugeda, M. M. *et al*. Observation of topologically protected states at crystalline phase boundaries in single-layer WSe$_2$. *Nat. Comm* **9**, 3401 (2018).
41. Chen, P. *et al*. Large quantum-spin-Hall gap in single-layer $1T'$ WSe$_2$. *Nat. Comm* **9**, 2003 (2018).
42. Tang, S. *et al*. Quantum spin Hall state in monolayer $1T'$-WTe$_2$. *Nat. Phys* **13**, 683–687 (2017).
43. Fei, Z. *et al*. Edge conduction in monolayer WTe$_2$. *Nat. Phys* **13**, 677–682 (2017).
44. Wu, S. *et al*. Observation of the quantum spin Hall effect up to 100 kelvin in a monolayer crystal. *Science* **359**, 76–79 (2018).
45. Jia, Z.-Y. *et al*. Direct visualization of a two-dimensional topological insulator in the single-layer $1T'$-WTe$_2$. *Phys. Rev. B* **96**, 041108(R) (2017).
46. Choe, D.-H., Sung, H.-J. & Chang, K. J. Understanding topological phase transition in monolayer transition metal dichalcogenides. *Phys. Rev. B* **93**, 125109 (2016).
47. Xu, H. *et al*. Observation of gap opening in $1T'$ phase MoS$_2$ nanocrystals. *Nano Lett.* **18**, 5085–5090 (2018).
48. Li, X., Zhang, S. & Wang, Q. Topological insulating states in 2D transition metal dichalcogenides induced by defects and strain. *Nanoscale* **9**, 562 (2017).
49. Nie, S. M., Song, Z., Weng, H. & Fang, Z. Quantum spin Hall effect in two-dimensional transition-metal dichalcogenide haeckelites. *Phys. Rev. B* **91**, 235434 (2015).
50. Vandenberghe, W. G. & Fischetti, M. V. Imperfect two-dimensional topological insulator field-effect transistors. *Nat. Comm* **8**, 14184 (2017).
51. Liu, Q., Liu, C.-X., Xu, C., Qi, X.-L. & Zhang, S.-C. Magnetic Impurities on the Surface of a Topological Insulator. *Phys. Rev. Lett.* **102**, 156603 (2009).
52. Kurilovich, V. D., Kurilovich, P. D. & Burmistrov, I. S. Indirect exchange interaction between magnetic impurities near the helical edge. *Phys. Rev. B* **95**, 115430 (2017).
53. Zheng, J.-H. & Cazalilla, M. A. Nontrivial interplay of strong disorder and interactions in quantum spin-Hall insulators doped with dilute magnetic impurities. *Phys. Rev. B* **97**, 235402 (2018).
54. Zhou, B., Lu, H.-Z., Chu, R.-L., Shen, S.-Q. & Niu, Q. Finite Size Effects on Helical Edge States in a Quantum Spin-Hall System. *Phys. Rev. Lett.* **101**, 246807 (2008).
55. Saha, D. & Mahapatra, S. Atomistic modeling of the metallic-to-semiconducting phase boundaries in monolayer MoS$_2$. *Appl. Phys. Lett.* **108**, 253106 (2016).
56. Saha, D. & Mahapatra, S. Asymmetric Junctions in Metallic-Semiconducting-Metallic Heterophase MoS$_2$. *IEEE Transactions on Electron Devices* **64**, 5 (2017).
57. QuantumATK with Virtual NanoLab, Synopsys Denmark, https://www.synopsys.com/silicon/quantumatk.html (Last accessed: 29 Aug 2019).
58. Perdew, J. P., Burke, K. & Ernzerhof, M. Generalized gradient approximation made simple. *Phys. Rev. Lett.* **77**, 3865 (1996).
59. Hamann, D. R. Optimized norm-conserving vanderbilt pseudopotentials. *Phys. Rev. B* **88**, 085117 (2013).
60. Schlipf, M. & Gygi, F. Optimization algorithm for the generation of oncv pseudopotentials. *Computer Physics Communications* **196**, 36–44 (2015).
61. Monkhorst, H. J. & Pack, J. D. Special points for Brillouin-zone integrations. *Phys. Rev. B* **13**, 5188 (1976).
62. Liu, D. C. & Nocedal, J. On the limited memory BFGS method for large scale optimization. *Math. Program.* **45**, 503–528 (1989).
63. Heyd, J., Scuseria, G. E. & Ernzerhof, M. Hybrid functionals based on a screened Coulomb potential. *J. Chem. Phys.* **118**, 8207–8215 (2003).
64. Kresse, G. & Furthmüller, J. Efficient iterative schemes for ab initio total energy calculations using a plane-wave basis set. *Phys. Rev. B* **54**, 11169 (1996).
65. Kresse, G. & Furthmüller, J. Efficiency of ab-initio total energy calculations for metals and semiconductors using a plane-wave basis set. *Comput. Mater. Sci.* **6**, 15–50 (1996).
66. Coleman, T. F. & Li, Y. An Interior, Trust Region Approach for Nonlinear Minimization Subject to Bounds. *SIAM Journal on Optimization* **6**, 418–445 (1996).

67. Coleman, T. F. & Li, Y. On the Convergence of Reflective Newton Methods for Large-Scale Nonlinear Minimization Subject to Bounds. *Mathematical Programming* **67**, 189–224 (1994).
68. Datta, S. *Electronic Transport in Mesoscopic Systems*. (Cambridge University Press, Cambridge, 1995).

Author contributions

B.D. performed the DFT calculations, developed the *k.p* Hamiltonian based continuum model and analyzed final results. D.S. helped in obtaining the edge state spectra. S.M. conceived the problem statement and overall supervised the work. All authors contributed in article writing.

Competing interests

The authors declare no competing interests.

Additional information

Supplementary information is available for this paper at https://doi.org/10.1038/s41598-020-63450-5.

Correspondence and requests for materials should be addressed to B.D.

Reprints and permissions information is available at www.nature.com/reprints.

Publisher's note Springer Nature remains neutral with regard to jurisdictional claims in published maps and institutional affiliations.